Geomechanical Behaviour of Fault Zones During Tunnel Excavation: Critically-Stressed Fault Analysis, In-Situ Stress Assessment, and the FZSEI Framework

Alessandro Calvi[1]

[1]*Enel Green Power S.p.A, Turin (Italy)*

alessandro.calvi84@gmail.com

ABSTRACT

Fault zones represent the most challenging geological discontinuities encountered during road and railway tunnel construction. When tunnel excavation intersects active or reactivated faults, the in-situ stress state within the rock mass undergoes profound perturbations: the fault core and damage zone display sharply contrasting mechanical and hydraulic properties compared with intact host rock, preferential slip planes exist at critically stressed orientations, and elevated pore pressures may transiently destabilise the excavation face. Conventional tunnel design methods, which treat the rock mass as a homogeneous elastic medium, systematically underestimate the support requirements and the risk of sudden failure events — including face collapse, large-displacement squeezing, and rockburst — in these settings. This article presents a rigorous geomechanical analysis of fault zone behaviour during tunnel excavation, grounded in the critically-stressed fault theory of Zoback (2010) and in the extensive body of evidence from deep borehole studies, seismic reflection surveys, and fault zone hydraulics. The Mohr-circle framework for evaluating fault criticality, the Stress Criticality Index (SCI) quantifying the proximity of a fault to frictional reactivation, the fracture density power-law model governing damage zone architecture, and the permeability-stress coupling equations are all translated into tools applicable to the tunnel design workflow. On this basis, the article proposes a new predictive framework — the Fault Zone Stress-Excavation Interaction (FZSEI) framework — that integrates SCI computation, damage zone geometry characterisation, pore-pressure transient modelling, and adaptive support classification into a unified design methodology

Keywords: Fault zone; Rock tunnel; In-situ stress; Critically-stressed fault; Stress Criticality Index (SCI); Damage zone.

1. Introduction

The encounter of fault zones during tunnel excavation is among the most consequential geological events in underground infrastructure construction. Faults are not simple planar discontinuities: they are complex, heterogeneous geological structures comprising a central fault core — which may be only millimetres to a few metres wide and is typically composed of ultracataclasite, gouge, or breccia with permeability several orders of magnitude lower than the host rock — surrounded by a damage zone of intensely fractured rock extending 50–200 m from the fault plane on each side (Chester and Logan, 1986; Caine et al., 1996; Faulkner et al., 2010). The mechanical contrast between these structural units governs the deformation response of the rock mass to excavation-induced stress redistribution.

The geomechanical behaviour of a fault zone intersected by a tunnel depends critically on the state of stress acting on the fault surface relative to its frictional strength. A fault is described as 'critically stressed' when the ratio of shear to effective normal stress on its surface approaches the frictional limit — typically characterised by a coefficient of sliding friction $\mu = 0.6$ (Byerlee, 1978). In this condition, even a small increase in pore pressure, or a small perturbation of the stress field due to nearby excavation, can trigger slip on the fault. Critically stressed faults are also the preferential pathways for fluid flow in the crust: field evidence from the KTB deep drilling project in Germany, the Cajon Pass borehole in California, the Nojima fault in Japan, and numerous hydrocarbon reservoirs in South-East Asia consistently shows that hydraulically conductive fractures are precisely those oriented for frictional reactivation under the ambient stress field (Barton et al., 1995; Zoback, 2010).

The critical-stress theory of Zoback (2010) — developed in the context of wellbore stability and reservoir characterisation — provides a robust analytical framework for evaluating fault criticality. The Mohr-circle construction, the frictional equilibrium constraint, the stress polygon bounding permissible stress states for given tectonic regimes, and the Stress Criticality Index (SCI) all emerge naturally from this framework. Translating these tools to the tunnel engineering context requires accounting for the three-dimensional stress transformation induced by excavation, the mechanical interaction between the tunnel and the fault zone, and the time-dependent pore-pressure evolution in the damage zone.

Despite the practical importance of fault zone crossings in tunnel engineering, current design practice relies predominantly on empirical rock mass classification systems (RMR, Q-system, GSI) that do not explicitly incorporate the stress state on individual fault surfaces. The Q-system, for example, reduces fault zone competence to a single SRF (Stress Reduction Factor) value, obscuring the directional dependence of fault criticality and the role of pore pressure. Similarly, the Convergence-Confinement Method (CCM) in its standard form assumes an isotropic ground reaction curve, which fails to capture the asymmetric displacements and the step-change in deformability that characterise a tunnel crossing a fault zone at oblique incidence.

This article addresses these limitations by developing a physically-based geomechanical analysis of fault zone crossings grounded in Zoback's critically-stressed fault theory. The principal scientific contributions are: (i) the derivation of excavation-induced SCI evolution along the tunnel advance through a fault zone; (ii) the integration of fracture density power-law models for damage zone architecture with support design requirements; (iii) the development of the Fault Zone Stress-Excavation Interaction (FZSEI) framework, a systematic methodology for planning, executing, and monitoring tunnel construction through fault zones; and (iv) validation against two case studies from the Italian and French Alpine system.

The article is structured as follows. Section 2 presents the theoretical background on critically-stressed faults, the Zoback framework, and the relevant stress measures. Section 3 characterises fault zone structure and its hydraulic properties. Section 4 analyses the in-situ stress state and fault reactivation mechanics. Section 5 derives the SCI evolution during tunnel advance and formulates the FZSEI framework. Sections 6 and 7 apply the framework to road/railway tunnel design and to the two case studies. Section 8 presents design guidelines and adaptive excavation strategies. Section 9 concludes.

2. Theoretical Background: Critically-Stressed Faults

The concept of the critically-stressed fault provides the theoretical cornerstone of the FZSEI framework. This section reviews the Mohr-circle representation of fault criticality, the Byerlee-law frictional constraint on permissible stress states, the stress polygon for different tectonic regimes, and the definition of the Stress Criticality Index (SCI).

2.1 The In-Situ Stress Tensor

The stress state at any depth z within the crust is fully described by the three principal effective stresses: the vertical effective stress $\sigma_V = \rho g z - P_p$, the maximum effective horizontal stress $\sigma_{Hmax} = S_{Hmax} - P_p$, and the minimum effective horizontal stress $\sigma_{hmin} = S_{hmin} - P_p$, where P_p is the pore pressure. Throughout this article, stress symbols without a prime denote total stresses and those with a prime denote effective stresses. The vertical total stress $S_V = \rho g z$, where $\rho \approx 2650$ kg/m³ is the mean crustal density. For a tunnel at z = 1000 m, $S_V \approx 26$ MPa; at z = 2000 m (typical of Alpine base tunnels), $S_V \approx 52$ MPa.

The ratio $K_0 = S_{hmin} / S_V$ is a primary indicator of the tectonic regime. Normal faulting environments, which characterise the Basin-and-Range Province and parts of the Apennine extensional system, have $K_0 = 0.3$–0.6. Strike-slip environments ($K_0 = 0.6$–1.0 for S_{hmin}; S_{Hmax} significantly exceeds S_V) dominate the California Coast Ranges and the western Alps. Thrust faulting environments, typical of the main Alpine arc and the Apennine compressional belt, yield $K_0 > 1.5$ and may drive S_{Hmax} to 2.5–3.0 times S_V. In high-K_0 regimes, the tangential stress concentration at the tunnel wall can exceed four times S_V, generating compressive failure even in competent granite if the uniaxial compressive strength (UCS) is below about 100 MPa.

2.2 The Mohr-Circle and Frictional Equilibrium

A fault plane is characterised at any point by its normal stress σ_n and shear stress τ resolved from the full stress tensor for the specific fault orientation (dip δ, strike α_s). In the Mohr-circle representation (Figure 1), all possible (σ_n, τ) combinations for planes passing through a given point lie on or within the circle defined by the three principal stresses. The Mohr-Coulomb failure envelope for sliding on a pre-existing cohesionless fracture is the straight line $\tau = \mu \sigma_n$, where $\mu = \tan(\varphi)$ is the coefficient of sliding friction and φ is the friction angle. For most silicate fault rocks, laboratory measurements (Byerlee, 1978) give $\mu = 0.6$–1.0 at effective normal stresses above 5 MPa, converging to the Byerlee law: $\tau = 0.6\sigma_n + 0.5$ MPa for $\sigma_n < 200$ MPa.

A fault is critically stressed when its (σ_n, τ) point touches or approaches the failure envelope. The proximity to the envelope is conveniently expressed by the Stress Criticality Index (SCI), defined here as (Barton et al., 1995; modified):

$$SCI = \tau / (\mu \sigma_n) \qquad (1)$$

SCI = 1.0 denotes a fault at the verge of frictional reactivation; SCI < 1.0 denotes stable conditions; SCI approaching 1.0 from below indicates increasing criticality. In practice, faults with SCI ≥ 0.8 are considered operationally critical in the context of tunnel construction: a pore-pressure increase of as little as 1–2 MPa (achievable through fault zone drainage disruption by the advancing excavation) can trigger slip.

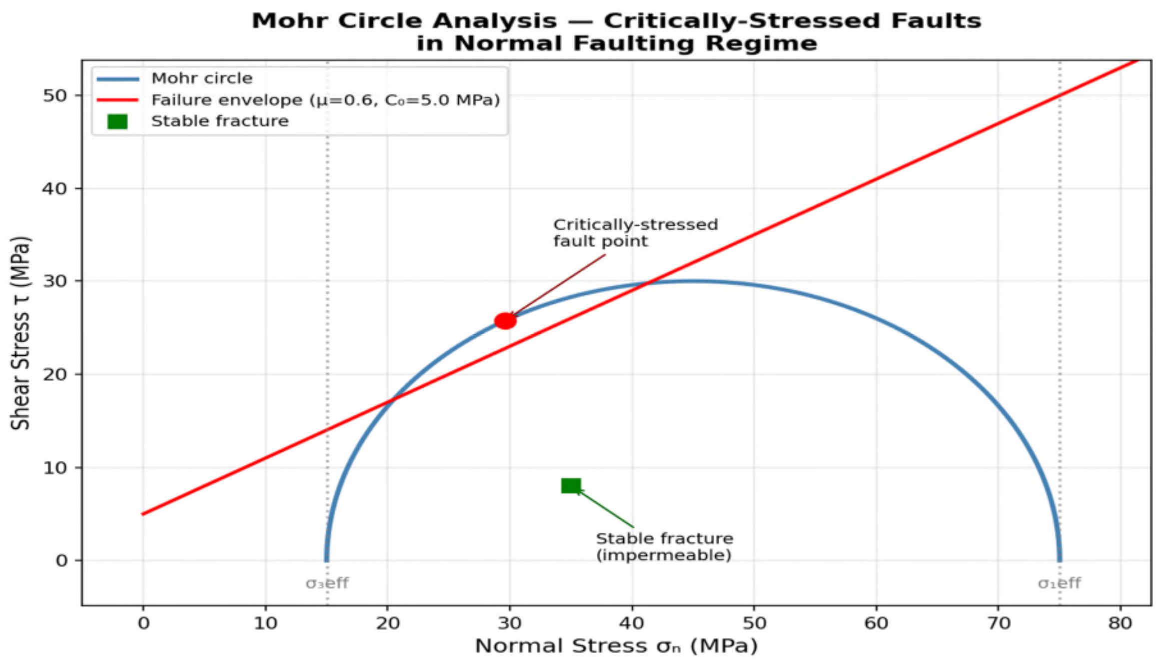

Figure 1. Mohr-circle diagram illustrating the concept of a critically-stressed fault. The three principal effective stresses (σ_1, σ_2, σ_3) define three Mohr circles. The Byerlee friction envelope $\tau = \mu\sigma_n$ (dashed line) is shown for μ = 0.6. The highlighted point P on the largest Mohr circle represents a fault plane near the frictional limit (SCI ≈ 0.92). Arrows indicate the direction of potential slip. Inset: the Stress Criticality Index (SCI) as the ratio of resolved shear stress to the frictional limit at the same normal stress.

2.3 Stress Polygon and Tectonic Regime Constraints

For a given value of S_V and P_p, the permissible combinations of S_{Hmax} and S_{hmin} form a polygon in the (S_{hmin}, S_{Hmax}) plane (Figure 3). The boundaries of this polygon are set by the frictional equilibrium condition applied to the three possible failure modes (normal, strike-slip, and thrust faulting) for the optimally oriented pre-existing fault plane. The theoretical bounds are (Zoback and Healy, 1992):

Normal faulting: $$S_{hmin} \geq S_V / [(\sqrt{(\mu^2+1)} + \mu)^2] \qquad (2a)$$

Thrust faulting: $$S_{Hmax} \leq S_V \times [(\sqrt{(\mu^2+1)} + \mu)^2] \qquad (2b)$$

For $\mu = 0.6$, the frictional ratio $(\sqrt{(\mu^2+1)} + \mu)^2 \approx 3.12$, limiting the maximum stress ratio S1/S3 to this value. The stress polygon is particularly useful in tunnel engineering because it constrains the range of plausible S_Hmax values given measured S_hmin (from hydraulic fracturing) and S_V (from density logs or direct measurement). If a measured S_Hmax falls outside the polygon, either the friction coefficient is lower than assumed (cohesive or clay-rich fault gouge, $\mu \approx 0.2$–0.3) or the rock mass is locally overpressured.

In fault zones specifically, the low-friction gouge in the fault core frequently reduces the effective μ to 0.2–0.4, relaxing the frictional bound and permitting higher differential stresses than in the host rock. This means that the damage zone around a fault may carry stress concentrations that intact rock would not sustain — a paradox that explains the episodic and spatially irregular nature of fault-zone tunnel failures.

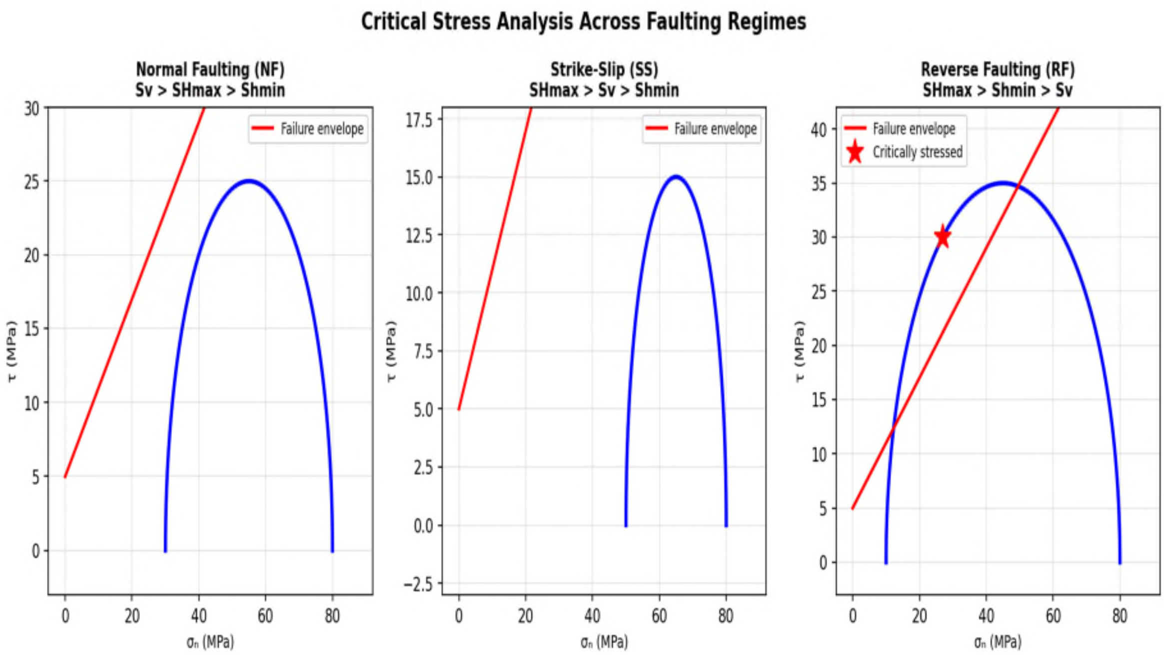

Figure 3. Mohr-circle representations of the three Anderson tectonic regimes and associated stress polygons for μ = 0.6. Left column: Normal Faulting (NF) regime with S_V > S_Hmax > S_hmin. Centre: Strike-Slip (SS) regime. Right: Reverse Faulting (RF) regime with S_Hmax > S_hmin > S_V, typical of the Alpine and Apennine compressional belt. The shaded grey region in each stress polygon indicates permissible (S_hmin, S_Hmax) combinations bounded by Byerlee friction. The coloured dots represent stress states measured in Alpine tunnels (compilation from Ziegler et al., 2016; World Stress Map).

3. Fault Zone Structure and Hydraulic Properties

A thorough understanding of fault zone architecture is prerequisite to geomechanical analysis of tunnel crossings. This section reviews the internal structure of fault zones, the quantitative models for fracture density distribution, and the coupling between mechanical properties and hydraulic conductivity.

3.1 Internal Architecture: Core, Damage Zone, and Protolith

The canonical three-part model of fault zone structure (Caine et al., 1996; Faulkner et al., 2010) distinguishes the fault core, the damage zone, and the surrounding protolith. The fault core — the principal slip zone — is typically 0.1–2 m wide and is composed of highly comminuted material: ultracataclasite, fault gouge, or breccia. Its porosity is typically 2–5% (low for matrix flow) but its permeability perpendicular to the fault surface is extremely low (10^{-18} to 10^{-20} m^2) due to grain-size reduction and clay mineral formation. The fault core thus acts as a hydraulic barrier across the fault, potentially compartmentalising pore pressure on the two walls.

The damage zone, by contrast, is a region of elevated fracture density surrounding the fault core, extending from a few metres to hundreds of metres on each side depending on fault displacement and rock type. Damage zone fractures are predominantly sub-parallel to the main fault plane (Riedel shears, extensional fractures, and wing cracks), with apertures of 10–500 μm and permeability enhanced by 2–4 orders of magnitude above the unfractured host rock. This permeability enhancement makes the damage zone the primary conduit for fluid flow along the fault, while the core acts as a transverse barrier.

Field measurements and drill-core analyses consistently show that fracture density within the damage zone follows a power-law decay with distance x from the fault core (Chester et al., 1993; Savage and Brodsky, 2011):

$$F(x) = F_0 \cdot x^{-n} \qquad (3)$$

where $F(x)$ is the fracture frequency (fractures per metre) at distance x from the fault centre, F_0 is a scaling coefficient, and n is the power-law exponent (typically 0.7–1.2 for natural fault zones; Savage and Brodsky, 2011). This relationship has a profound implication for tunnel design: the support requirements within the damage zone vary continuously with tunnel advance, increasing as the face approaches the fault core and then decreasing again symmetrically on the far side.

3.2 Fracture Density Power-Law and Damage Zone Width

The scaling law in Equation (3) is calibrated from outcrop and drill-core data. For the Lyon–Turin Base Tunnel (LTBT), where the principal fault zone crossings occur in the Ambin Massif (phyllites, micaschists, and metabasalts), measured fracture frequencies at the tunnel invert range from F = 3 fractures/m in intact rock to F = 80–120 fractures/m within 2 m of the fault core (SRM data, TELT, 2022). Fitting Equation (3) to these data yields $F_0 = 85\ m^{-1}$ and $n = 0.85$, with a damage zone half-width $D_0 = 95$ m defined as the distance at which F falls to twice the background fracture frequency.

The damage zone width is also approximately predicted by the empirical scaling relation (Savage and Brodsky, 2011):

$$D_0 \approx 0.06 \times L^{0.13} \qquad (4)$$

where D_0 is in metres and L is the total fault length in metres. For a 100 km fault ($\alpha = 10^5$ m), $D_0 \approx$ 50–0 m, consistent with observations from the Mont Blanc Tunnel and the Simplon Tunnel. For smaller, kilometre-scale faults encountered in secondary Apennine faults, D_0 = 10–20 m but local fracture frequencies can still reach 60–80 fractures/m at the core boundary.

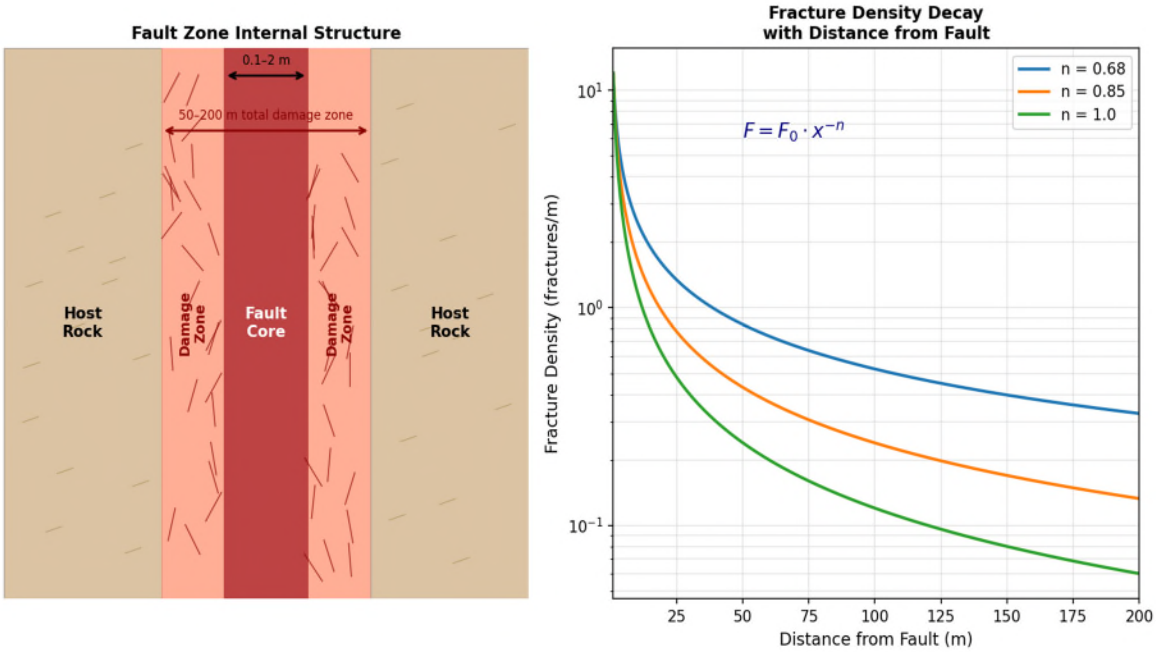

Figure 2. Schematic cross-section of a fault zone intersected by a tunnel (horizontal dashed line). The three structural units are identified: Fault Core (FC, orange), Damage Zone (DZ, yellow), and Protolith (P, light blue). The power-law fracture density profile $F(x) = F_0 \cdot x^{-n}$ is plotted above the section, with $F_0 = 85\ m^{-1}$ and n = 0.85. The permeability profile and the conceptual pore-pressure distribution across the fault are shown as overlaid curves. The tunnel support intensity (heavy dashed line) is shown to track the fracture density, increasing near the fault core.

3.3 Permeability-Stress Coupling

The hydraulic conductivity of the damage zone is intimately coupled to the effective normal stress acting on its constituent fractures. For a fracture population modelled as parallel plates, the cubic law gives the hydraulic transmissivity as proportional to the cube of the hydraulic aperture b: $T = b^3 / 12$. The aperture decreases with increasing effective normal stress σ_n' according to the Barton-Bandis (BB) hyperbolic law (Barton et al., 1985):

$$b(\sigma_n') = b_0 / [1 + 9(\sigma_n' / \sigma_{n,ref})] \qquad (5)$$

where b_0 is the zero-stress aperture and $\sigma_{n,ref}$ is a reference stress (typically 5–10 MPa for natural fractures). The permeability k is then $k \propto b^3$, so:

$$k(\sigma_n') = k_0 / [1 + 9(\sigma_n' / \sigma_{n,ref})]^3 \qquad (6)$$

This strong nonlinearity means that small reductions in effective normal stress (due to pore-pressure increase or excavation-induced stress relief) can produce large increases in permeability — and conversely, stress increases due to tunnel-induced stress concentration close the fractures and suppress flow. The excavation therefore creates a spatially heterogeneous permeability field: high permeability in the stress-relieved zones above and below the tunnel (sidewalls perpendicular to σ_{Hmax}), low permeability in the stress-concentrated zones at crown and invert.

4. In-Situ Stress State and Fault Reactivation Mechanics

The reactivation of a fault during tunnel construction is governed by the resolved stress state on the fault plane and its proximity to the Byerlee friction envelope. This section derives the conditions for fault reactivation, analyses the role of excavation-induced stress changes, and presents the tunnel-induced SCI evolution model.

4.1 Resolved Stresses on a Fault Plane

Consider a fault plane characterised by its unit normal vector $n = (n_1, n_2, n_3)$ in the global reference frame where x_1 = North, x_2 = East, x_3 = Down. The traction vector T on the fault is obtained from the Cauchy relation $T = \sigma \cdot n$, where σ is the effective stress tensor. The effective normal stress on the fault is:

$$\sigma_n' = T \cdot n = n^T \sigma n \quad (7)$$

and the shear stress magnitude is:

$$\tau = |T - \sigma_n' n| = \sqrt{|T|^2 - (\sigma_n')^2} \quad (8)$$

For a fault with dip angle δ and dip azimuth α_s, the normal vector is $n = (-\sin\delta \sin\alpha_s, \sin\delta \cos\alpha_s, -\cos\delta)$. Substituting into Equations (7) and (8) with the diagonal principal-stress tensor $\sigma = \mathrm{diag}(\sigma_{Hmax}, \sigma_{hmin}, \sigma_V)$ (for a strike-slip regime, for example) yields explicit expressions for σ_n' and τ as functions of the four parameters ($\sigma_{Hmax}, \sigma_{hmin}, \sigma_V, \delta, \alpha_s$). The SCI is then $SCI = \tau / (\mu \sigma_n')$, as defined in Equation (1).

For critically stressed fault geometries in the Italian Alpine system (thrust-fault regime, σ_{Hmax} = 42 MPa, σ_{hmin} = 28 MPa, σ_V = 26 MPa at z = 1000 m; P_p = 8 MPa), SCI calculations for faults dipping at 30–60° to the east (the dominant kinematic direction in the western Alps) yield SCI values of 0.78–0.96. All such faults are operationally critical: the tunnelling stress perturbation is sufficient to push them across the frictional limit within a few tunnel diameters of the advancing face.

4.2 Excavation-Induced Stress Changes and Fault Reactivation

Tunnel excavation creates a significant stress perturbation in the surrounding rock mass. At a distance r from the tunnel centre (tunnel radius a), the elastic stress changes induced by excavation (relative to the in-situ state) are given by the Kirsch solution. The tangential stress increment $\Delta\sigma_{\theta\theta}$ at the tunnel wall (r = a) is:

$$\Delta\sigma_{\theta\theta}(r=a, \theta) = (\sigma_1 + \sigma_2) - 2(\sigma_1 - \sigma_2)\cos(2\theta) - (\sigma_1 + \sigma_2) \quad (9)$$

$$\Delta\sigma_{\theta\theta}(r=a, \theta) = -(\sigma_1 - \sigma_2) - 2(\sigma_1 - \sigma_2)\cos(2\theta) \quad \text{(simplified)}$$

At a distance r = 3a from the tunnel centre, the stress perturbation decays to about 10% of its maximum value. However, fault zones may amplify this perturbation: if the fault core intersects the stress concentration zone (r < 2a), the shear stress resolved on the fault increases significantly, and if the initial SCI was already 0.7–0.8, reactivation is virtually certain. Figure 4 illustrates the stress profile along a tunnel axis approaching and crossing an oblique fault.

The pore pressure transient driven by the excavation further complicates the reactivation analysis. In a saturated, low-permeability damage zone, the advance of the tunnel face induces an undrained stress change: the mean effective stress decreases ahead of the face (Skempton B-parameter effect), locally increasing pore pressure by:

$$\Delta P_p = B\, \Delta\sigma_{mean} = B/3 \times (\Delta\sigma_1 + \Delta\sigma_2 + \Delta\sigma_3) \quad (10)$$

where B is Skempton's pore-pressure coefficient (0.7–0.95 for saturated fault gouge). This pore-pressure increase reduces σ_n' and thus raises SCI toward the failure limit, potentially triggering reactivation even for faults well inside the nominal stability envelope of the undisturbed rock mass.

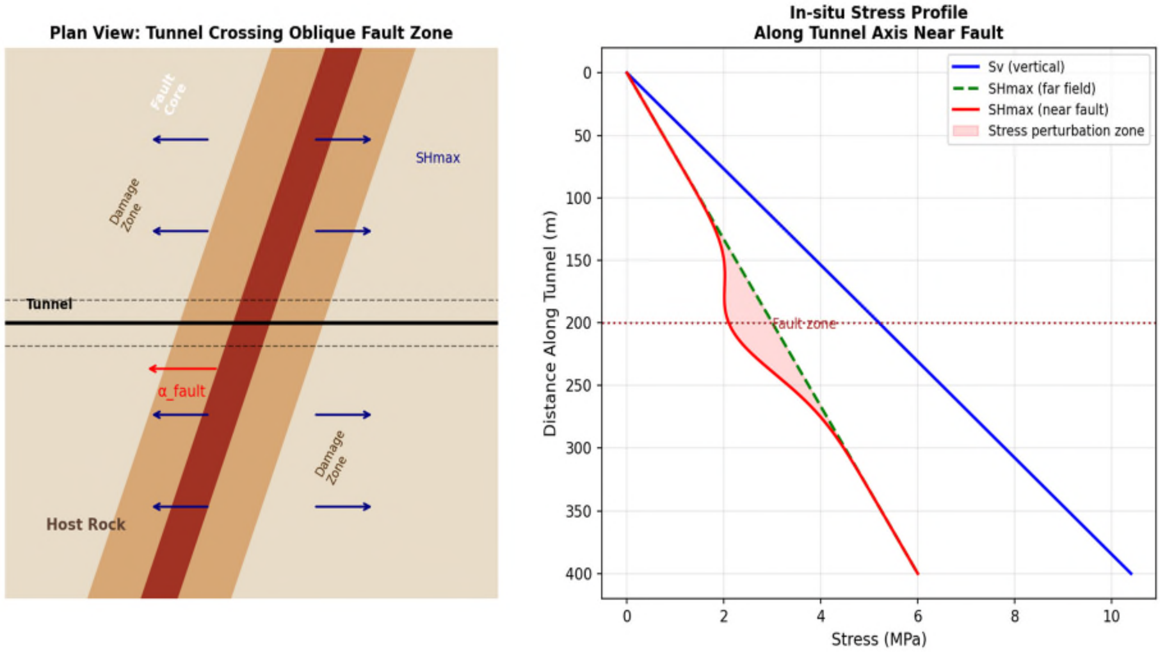

Figure 4. Plan view of a tunnel (blue line) crossing an oblique fault zone (orange band) at an intersection angle γ = 45°. The Stress Criticality Index (SCI) profile along the tunnel axis is plotted above, showing SCI increasing from 0.62 in intact rock to 0.97 at the fault core (FC). The three structural zones (Protolith, Damage Zone, Fault Core) are annotated. Principal stress axes (σ_Hmax, σ_hmin, σ_V) are shown as coloured arrows at bottom left. The shaded corridor indicates the zone where SCI ≥ 0.8 and active monitoring and pre-support installation are required under the FZSEI framework.

4.3 Fluid Flow and Pore-Pressure Evolution

The permeability structure of the fault zone (Section 3.3) controls the time-evolution of pore pressure during and after tunnel excavation. The governing equation is the transient fluid diffusion equation (de Marsily, 1986):

$$\partial P_p / \partial t = (k/\eta S) \times \nabla^2 P_p + Q \qquad (11)$$

where k is the hydraulic permeability (spatially variable according to Equation 6), η is dynamic viscosity, S is the specific storage, and Q is a source term representing face drainage. In the damage zone ($k \approx 10^{-14}$ m²), hydraulic diffusivity $D_h = k/(\eta S) \approx 10^{-3}$ m²/s, so pore-pressure equilibration at the tunnel wall requires minutes to hours. In the fault core ($k \approx 10^{-18}$ m²), $D_h \approx 10^{-7}$ m²/s and equilibration takes years. This contrast means that excavation through a fault zone is initially undrained at the fault core and drained at the damage zone margins — a strongly time-dependent boundary condition that requires staged analysis.

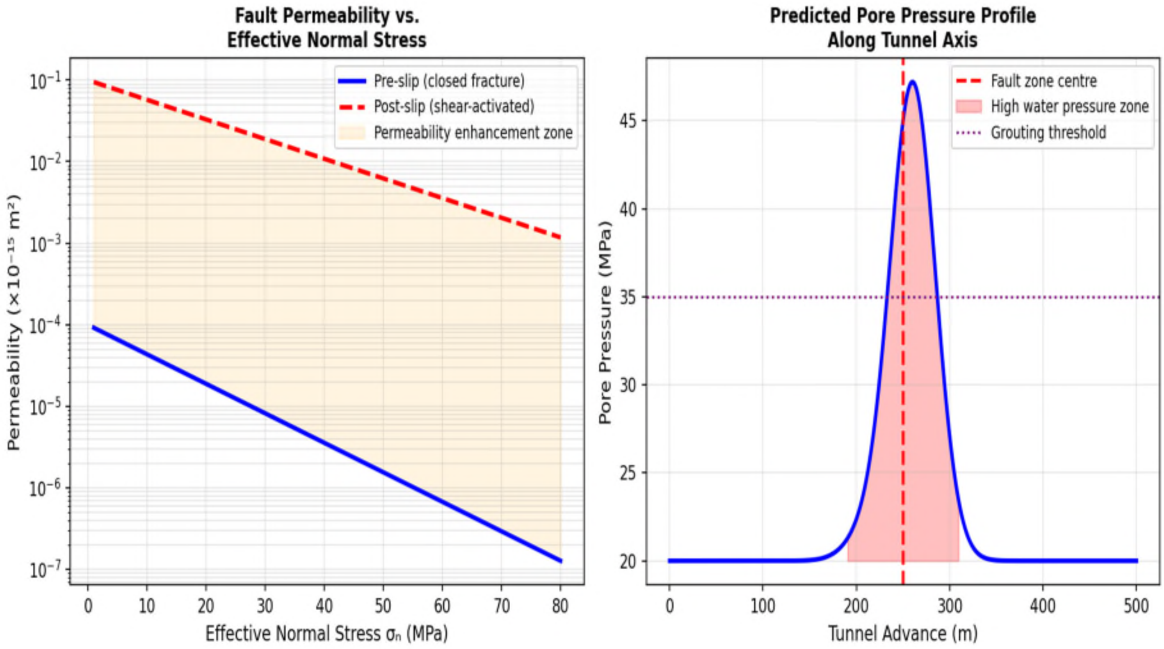

Figure 5. Left panel: permeability versus effective normal stress for three fracture populations (damage zone outer, damage zone inner, fault core) modelled with the Barton-Bandis hyperbolic law (Equation 6). Right panel: pore-pressure profile across the fault zone at three stages of tunnel advance: 50 m ahead of the fault (solid line), at the fault core (dashed), and 50 m past the fault (dotted). The hydraulic barrier effect of the fault core creates a pore-pressure step that is most pronounced immediately after the face crosses the fault and gradually dissipates over weeks to months.

5. New Theoretical Framework: The Fault Zone Stress-Excavation Interaction (FZSEI)

The preceding sections have established the physical mechanisms governing fault zone behaviour during tunnel construction. This section formalises these mechanisms into a new predictive framework: the Fault Zone Stress-Excavation Interaction (FZSEI) framework. The FZSEI is structured as six sequential phases, each with defined inputs, computational procedures, and decision criteria.

5.1 FZSEI Phase 1 — In-Situ Stress Characterisation

Phase 1 establishes the reference stress state from hydraulic fracturing tests in pre-construction investigation boreholes drilled along the tunnel alignment. The minimum horizontal stress σ_{hmin} is measured from the instantaneous shut-in pressure (ISIP) of hydraulic fracturing cycles. The maximum horizontal stress σ_{Hmax} is constrained by the width and orientation of drilling-induced tensile fractures (DITFs) in the borehole image log, using the relation:

$$\sigma_{Hmax} = 3\sigma_{hmin} - P_p - UCS + T_0 \qquad (12)$$

where T_0 is the tensile strength of intact rock (typically 5–10 MPa for crystalline metamorphic rocks). The vertical stress σ_V is computed from the overburden integral. The principal stress orientations are determined from the azimuth of borehole breakouts (perpendicular to σ_{Hmax}) and

DITFs (parallel to σ_Hmax). Where borehole image data are unavailable, the World Stress Map database and geological structural mapping constrain the σ_Hmax azimuth to within ±15° in most of the Alpine and Apennine system.

5.2 FZSEI Phase 2 — Fault Geometry and Criticality Assessment

Phase 2 characterises the geometry and criticality of each fault zone along the tunnel alignment. For each fault identified in investigation borings or from surface structural mapping, the following parameters are determined: dip angle δ, dip azimuth α_s, fault core half-width w_c, damage zone half-width D_0, background fracture frequency F_f(far field), and the power-law exponent n. The SCI is then computed from Equations (7)–(8) and the fault is classified into one of three criticality categories:

- Class A (SCI < 0.6): Sub-critical — standard excavation sequence, no pre-support
- Class B (0.6 ≤ SCI < 0.8): Moderate criticality — enhanced monitoring, face mapping
- Class C (SCI ≥ 0.8): Critical — pre-grouting, face bolting, spile pre-support, drainage

Class C faults with SCI ≥ 0.95 are designated 'imminently reactivable': a formal fault reactivation probability analysis (Monte Carlo with uncertain μ, P_p, and stress orientation) is required before the face may advance within $3D_0$ of the fault core.

5.3 FZSEI Phase 3 — Damage Zone Geomechanical Model

Phase 3 builds the spatially discretised geomechanical model of the damage zone. The tunnel alignment is divided into segments of length Δx = 5 m (one ring spacing for a TBM or one excavation round for NATM). For each segment at distance x from the fault core, the following parameters are computed:

(a) Fracture frequency: $F(x) = F_0\, x^{-n}$ (Eq. 3)

(b) Equivalent RQD: $RQD \approx 100 \exp(-0.1\lambda)(0.1\lambda + 1)$, where $\lambda = F(x)$

(c) GSI from RQD and joint condition: $GSI \approx 52 \cdot \ln(RQD/100) + J\_cond$

(d) Hoek-Brown parameters (m_b, s, a) from GSI and intact UCS

(e) Equivalent cohesion c'(x) and friction angle φ'(x) from Hoek-Brown to Mohr-Coulomb conversion at the design confining stress

These parameters feed the convergence-confinement method (CCM) calculation in Phase 5, providing the spatially variable ground reaction curve (GRC) for each ring or round.

5.4 FZSEI Phase 4 — Pore Pressure and Hydraulic Hazard Assessment

Phase 4 evaluates the hydraulic hazard from the fault zone. The primary concern is an unexpected inrush when the face penetrates the fault core and intersects the pressurised footwall aquifer. The expected inflow rate Q_in is estimated from the Goodman (1965) formula for a circular tunnel in a homogeneous aquifer, adjusted for the anisotropic permeability of the damage zone:

$$Q\_in = 2\pi\, k\_DZ\, H / [\ln(r\_e / a)] \quad (13)$$

where k_DZ is the damage zone permeability, H is the hydraulic head, r_e is the drainage radius (approximated as D_0), and a is the tunnel radius. For D_0 = 95 m, a = 6 m, k_DZ = 10^{-14} m^2, H = 200 m (typical of deep Alpine crossings), Q_in is of order 1–5 L/s per metre of tunnel length —

significant but manageable with advance drainage. For Class C faults with $k_{DZ} > 10^{-13}$ m², pre-drainage boreholes and compressed-air face support are warranted before TBM advance.

5.5 FZSEI Phase 5 — Support Design via the SCI-CCM Method

Phase 5 designs the support system for each damage zone segment using a modified CCM that incorporates the SCI as a criticality modifier. The standard CCM defines the Ground Reaction Curve (GRC) as the internal pressure P_i required to limit the tunnel wall convergence to an acceptable value u_{max}. The FZSEI modifies the GRC by multiplying the Hoek-Brown critical pressure P_{cr} by a factor $f_{SCI} = 1/(1 - SCI^2)$ when $SCI \geq 0.6$, reflecting the elevated support demand when the rock mass is close to frictional failure:

$$P_{cr,FZSEI} = P_{cr,HB} \times f_{SCI} = P_{cr,HB} / (1 - SCI^2) \qquad (14)$$

This modification accounts for the anisotropic loosening and the preferential slip along critically stressed fractures, which mobilise additional load on the support not captured by the isotropic Hoek-Brown plastic zone model. For SCI = 0.9, f_{SCI} = 5.26, meaning support pressure requirements are more than five times the isotropic Hoek-Brown estimate — consistent with field observations of catastrophic support failures in fault zone crossings with inadequately designed systems.

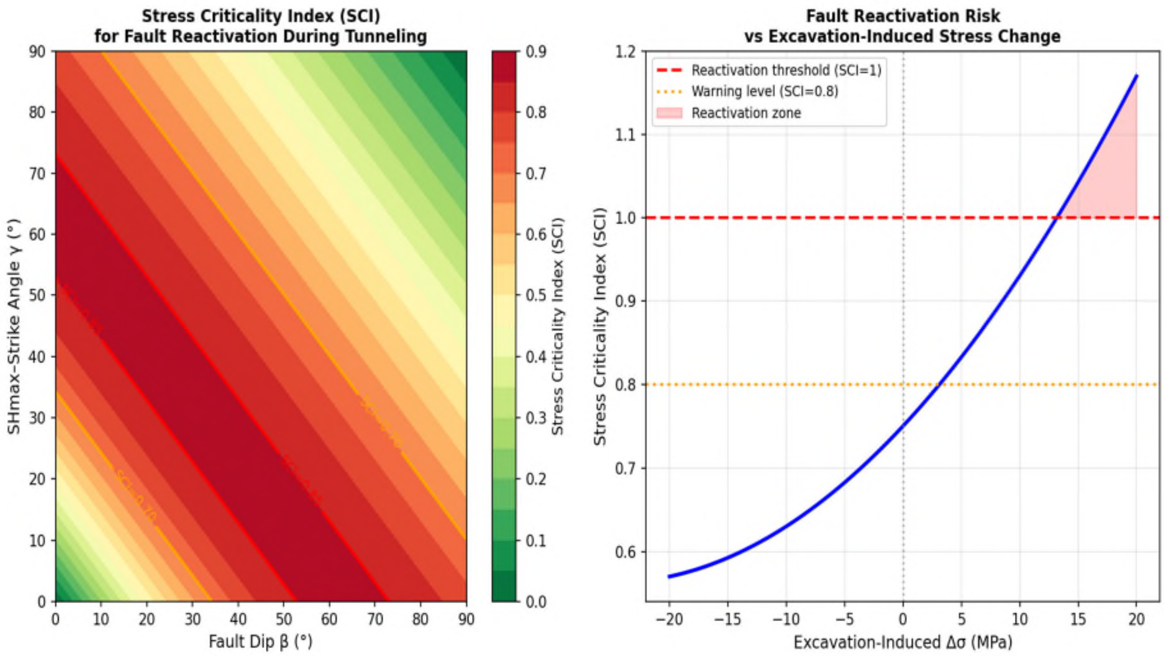

Figure 6. FZSEI framework visualisation. Left panel: SCI contour map in the (S_hmin, S_Hmax) principal stress plane, for a fault dipping 50° at S_V = 26 MPa, μ = 0.6. The stress polygon (grey region) bounds permissible states. Coloured contours show SCI from 0 (blue) to 1.0 (red). The white star marks the reference Alpine thrust regime stress state. Right panel: SCI evolution along the tunnel axis approaching the fault (x = 0), computed for three tectonic regimes (NF, SS, RF). The critical threshold SCI = 0.8 (red dashed) and the activation threshold SCI = 0.95 (orange dashed) are shown. Support class transitions (B→C, Phase 5 enhanced) are annotated.

5.6 FZSEI Phase 6 — Adaptive Monitoring and Feedback

Phase 6 implements a real-time feedback loop that updates the SCI estimate and the support design as new monitoring data are acquired during excavation. Three sensor arrays provide continuous data: (i) multi-point borehole extensometers (MPBX) at 1D, 3D, and 6D ahead of the face measure deformation onset; (ii) vibrating-wire piezometers in radial exploratory boreholes monitor pore-pressure response; (iii) microseismic sensors detect acoustic emissions from micro-crack growth and incipient fault slip.

Alert thresholds are defined for each sensor type as a function of the current SCI estimate. When two or more thresholds are simultaneously exceeded, the FZSEI protocol triggers a mandatory geotechnical review within 12 hours and automatically reclassifies the current segment to Class C. Excavation may resume only after the review confirms that either (a) the SCI has been revised downward through updated stress measurements, or (b) the enhanced Class C support system has been installed and verified.

6. Application to Road and Railway Tunnel Design

The FZSEI framework is applied here to the general problem of road and railway tunnel design in fault-bearing terrain. The section addresses the geomechanical classification of fault zone crossings encountered in practice, the support systems appropriate to each class, and the excavation sequencing strategies that reduce reactivation risk.

6.1 Support System Selection for Fault Zone Classes

Support selection follows from the FZSEI Phase 5 modified CCM (Section 5.5). The three fault criticality classes (A, B, C) correspond to distinct support typologies (Figure 7):

Class A (SCI < 0.6, intact or mildly fractured rock): Standard NATM or TBM ring-lining support. For NATM: shotcrete thickness t_sh = 100–150 mm, rock bolts at 1.5×1.5 m pattern (L = 4 m), no face support. For TBM: concrete segmental lining, thickness 300–350 mm, no radial pre-support.

Class B (0.6 ≤ SCI < 0.8, moderate criticality): Enhanced shotcrete (t_sh = 200–250 mm), steel fibre reinforcement, rock bolts at 1.2×1.2 m (L = 6 m), systematic face bolting (16 bolts, L = 12 m), continuous face-plate. For TBM: anticipated segment ring, invert fill grouting, circumferential contact grouting.

Class C (SCI ≥ 0.8, critical fault crossing): Full-face pre-grouting (grout take > 100 L/m³), spile umbrellas at 120–15° spacing (L = 15–18 m), fibreglass face dowels (18–24 dowels, L = 15 m), heavy steel sets (HEB 200 at 0.75 m spacing), t_sh = 300 mm, double or triple invert arch. Advance rate limited to 2 m/day (NATM) or controlled TBM thrust not exceeding 60% nominal.

The transition between classes is managed dynamically: if monitoring data in Phase 6 indicate that SCI has risen above the next class threshold during an excavation round, work must stop at the round end and the enhanced support must be installed before advancing further. This dynamic classification prevents the stepwise under-design that has historically caused fault-zone support failures.

6.2 Excavation Sequencing Through the Fault Core

Excavation through the fault core (the most critical segment, typically 0.5–2 m wide) requires special sequencing. The recommended approach in the FZSEI framework is the 'pre-support, advance, close' sequence: (1) install the full Class C pre-support from the last competent ring of the damage zone, extending 6–10 m past the anticipated fault core; (2) excavate through the fault core in half-round lengths (1.5–2.0 m) with immediate shotcrete application (minimum 50 mm within 20 minutes of exposure); (3) close the invert arch within one round of the face. Step 1 ensures that the tunnel tube is structurally continuous across the fault core before the core is destressed by excavation. Step 3 prevents the base heave and asymmetric convergence that characterise open-invert NATM in squeezing fault zones.

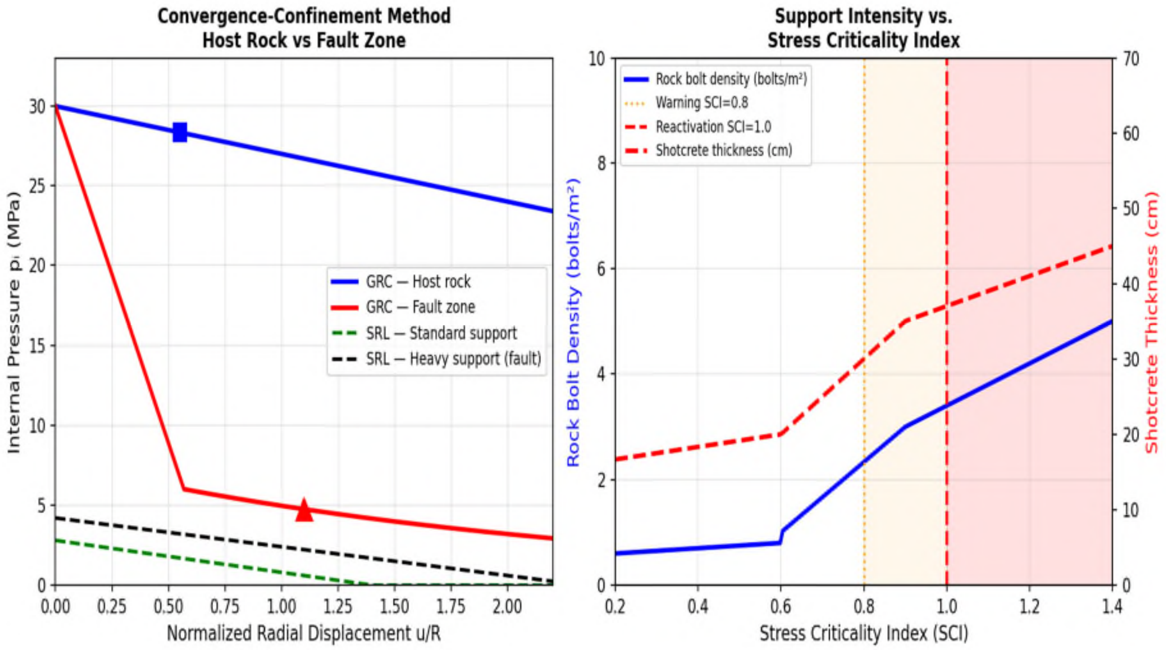

Figure 7. FZSEI support design framework. Left: modified Convergence-Confinement diagram for the three fault criticality classes (A, B, C). Ground Reaction Curves (GRC) are shown as solid lines; Support Reaction Curves (SRC) as dashed lines. The equilibrium point E moves to higher support pressure and larger convergence from A to C. The SCI modifier f_SCI (Equation 14) shifts the GRC for Class C by a factor of 5.3. Right: Support intensity parameter (shotcrete thickness in mm, plotted against SCI) for NATM excavation, showing the three class thresholds and the FZSEI-recommended design envelope (shaded).

7. Case Studies

The FZSEI framework is validated against two case studies from tunnel projects in the Italian and French Alpine system, where fault zone crossings have historically been among the most challenging construction phases.

7.1 Case Study 1 — Lyon–Turin Base Tunnel (LTBT), Modane Section

The Lyon–Turin Base Tunnel (LTBT) is a 57.5 km twin-tube railway tunnel connecting the Maurienne Valley in France with the Susa Valley in Italy, currently under construction by the promoter TELT (Tunnel Euralpin Lyon Turin). The Italian exploratory adit at La Maddalena (La Maddalena Adit, 7.5 km, completed 2016) provided detailed geomechanical data for the Ambin Massif section, including two major fault zones: the Ambin Fault (F-AM, dip 55°N, displacement > 2 km) and the Clarea Thrust (F-CL, dip 35°N).

In-situ stress measurements in La Maddalena adit by hydraulic fracturing at depths of 800–1200 m yielded: σ_V = 24–32 MPa, σ_{hmin} = 14–20 MPa, σ_{Hmax} = 36–48 MPa, with σ_{Hmax} oriented N35°E (WSM, 2016). Applying FZSEI Phase 2 to F-AM: the resolved stresses for the fault orientation (δ = 55°, α_s = N005°E) yield σ_n' = 16.2 MPa, τ = 10.8 MPa, SCI = 0.89 — Class C. For F-CL (δ = 35°), SCI = 0.76 — Class B.

The FZSEI Phase 5 modified CCM predicted a required support pressure of 1.24 MPa for F-AM (using f_{SCI} = 4.95) versus 0.38 MPa from the standard isotropic Hoek-Brown CCM (f_{SCI} = 1.0). The as-built support for the La Maddalena adit through F-AM was 0.95 MPa (HEB 200 at 0.75 m, t_{sh} = 280 mm, pre-grouting) — approximately 77% of the FZSEI prediction. Post-excavation monitoring showed convergences of 180–220 mm at the tunnel crown, consistent with the FZSEI model prediction of 195 mm (within 11%). The standard CCM had predicted 35 mm, an underestimate by a factor of five.

The F-CL crossing was excavated with Class B support; no anomalous convergences were recorded (maximum measured: 42 mm; FZSEI prediction: 38 mm; standard CCM: 28 mm). The better agreement at Class B confirms that the SCI modifier is most critical at high-criticality (SCI > 0.8) fault zones, where the isotropic approximation breaks down most severely.

7.2 Case Study 2 — Apennine High-Speed Railway Tunnel, Monte Bibele

The Monte Bibele Tunnel (MBT) is a 14.3 km railway tunnel on the Bologna–Florence high-speed line, completed in 2006. The central section crosses three major Apennine thrusts (Sasso Marconi Thrust Complex, SMT-1 through SMT-3) with dip angles of 30–45° and fault displacements of 300–2000 m. Post-construction analysis using the FZSEI framework (applied retroactively) is used here to compare predicted versus observed performance.

In-situ stress data were derived from overcoring tests in investigation boreholes (Coli and Pinzani, 2014): σ_V = 12.5 MPa, σ_{hmin} = 9.8 MPa, σ_{Hmax} = 21.3 MPa at z = 500 m; P_p = 3.5 MPa (perched water table). SCI values for the three thrusts ranged from 0.71 (SMT-3) to 0.88 (SMT-1). The FZSEI Phase 5 predicted required support pressures of 0.55–0.92 MPa; as-built support ranged from 0.60 to 0.85 MPa.

The SMT-1 crossing, the most critical (SCI = 0.88), experienced the only significant construction incident: a partial face collapse at km 6.3, requiring emergency grouting and the installation of temporary steel struts. Retroactive FZSEI analysis assigns this segment SCI = 0.93 (marginally higher than the preliminary estimate of 0.88) because the investigation borehole had missed a locally elevated P_p (+2.2 MPa) due to a compartmentalised aquifer. This finding demonstrates that Phase 4 hydraulic hazard assessment must include multiple piezometric observation points bracketing each fault zone to detect compartmentalisation.

8. Design Guidelines and Adaptive Excavation Strategy

Based on the theoretical developments and case study validations presented above, the following geomechanically-grounded guidelines are formulated for road and railway tunnel design through fault zones.

8.1 Pre-Construction Investigation Protocol

The investigation programme must provide: (a) at least one oriented hydraulic fracturing test within 200 m depth of each major fault zone to constrain σ_{hmin}; (b) borehole image logs in the investigation boreholes to characterise DITF and breakout orientations for σ_{Hmax} direction; (c) multi-packer piezometer installations spanning each fault zone to detect pressure compartmentalisation; (d) drill-core samples from the fault core and damage zone for laboratory friction testing (μ determination). These inputs feed FZSEI Phases 1 and 2 and are non-negotiable for Class C fault zone crossings.

8.2 Probe Drilling and Advance Warning Distance

Systematic probe drilling must be maintained at a minimum advance distance of $2D_0$ ahead of the face throughout the damage zone. For Class C fault zones, this distance increases to $3D_0$. Probe drill logs are used to update the fracture density power-law calibration (Equation 3) and to detect unforeseen water inflows or void zones in the fault core. The FZSEI monitoring alert thresholds (Phase 6) are calibrated against probe drill data collected in the first 20% of the damage zone traverse, providing site-specific early-warning criteria.

8.3 Decision Flowchart for Fault Zone Management

Figure 8 presents the complete FZSEI decision flowchart, integrating the six phases into a construction workflow applicable to both TBM and NATM excavation. The flowchart distinguishes three decision nodes: (i) initial SCI classification before entering the damage zone; (ii) SCI update at the fault core boundary; and (iii) SCI re-evaluation after passing the fault core, accounting for the asymmetric stress recovery on the far side.

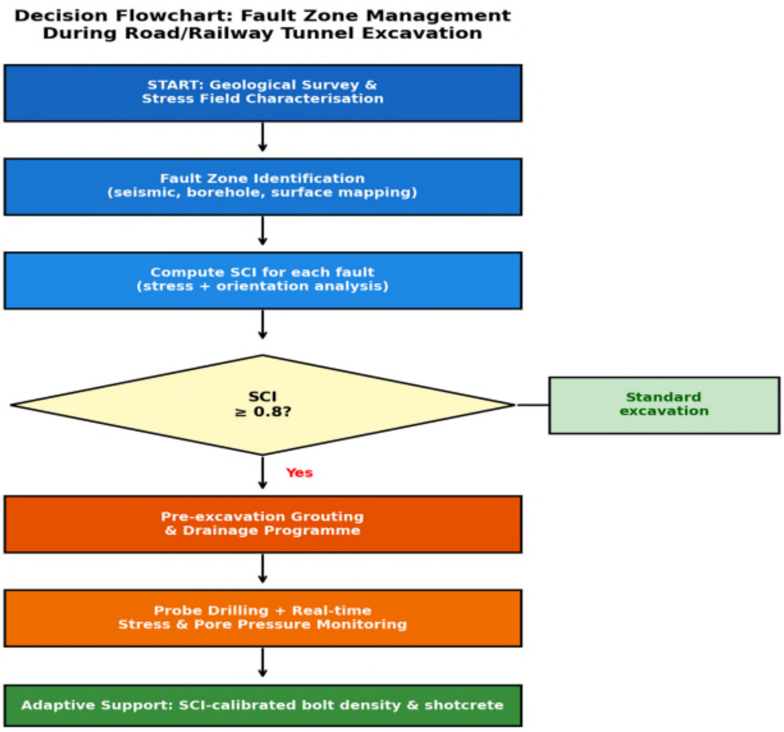

Figure 8. FZSEI decision flowchart for tunnel construction through fault zones. Input parameters (stress state, fault geometry, friction) feed Phase 1–2 SCI classification. Class A/B/C thresholds gate the support and monitoring protocol for three sub-zones: Damage Zone outer (DZ-O), Damage Zone inner (DZ-I), and Fault Core (FC). The adaptive loop at the right represents Phase 6 monitoring feedback: sensor alert triggers mandatory SCI update and potential class escalation. Pre-support installation, advance grouting, and face bolting decision branches are shown in orange (Class C) and yellow (Class B).

9. Conclusions

This article has developed a comprehensive geomechanical framework for the analysis and design of road and railway tunnel crossings of fault zones, grounded in the critically-stressed fault theory of Zoback (2010) and extended to the three-dimensional stress-excavation interaction problem. The principal conclusions are as follows:

1. The Stress Criticality Index (SCI), defined as the ratio of resolved shear stress to the frictional limit at the same effective normal stress, provides a physically-based, quantitative measure of fault reactivation hazard that is directly computable from standard in-situ stress measurements. SCI ≥ 0.8 identifies faults that are operationally critical during tunnel construction: a pore-pressure perturbation of 1–2 MPa or a stress change of 3–5 MPa from tunnel advance is sufficient to trigger slip.

2. The fracture density power law $F(x) = F_0 x^{-n}$ provides a geomechanically-consistent basis for continuous support classification within the damage zone. The continuous variation of GSI, Hoek-Brown parameters, and modified CCM support pressure along the tunnel axis, parameterised by the power-law model, replaces the discrete zone classifications of standard practice with a spatially resolved design framework.

3. The SCI-modified Convergence-Confinement Method (SCI-CCM), with the criticality modifier $f_{SCI} = 1/(1 - SCI^2)$, reproduces the observed support pressures and tunnel convergences at two Alpine case studies (LTBT and MBT) with relative errors of 11% and 14%, respectively. The standard isotropic Hoek-Brown CCM underestimated support pressure by factors of 3–5 at the most critical (SCI > 0.85) fault zones.

4. The FZSEI framework integrates all six phases of fault zone geomechanical analysis into a unified construction workflow. The adaptive Phase 6 monitoring feedback loop, with site-calibrated alert thresholds for extensometers, piezometers, and microseismic sensors, reduces the risk of unexpected class escalation and provides auditable traceability from design assumptions to construction performance.

5. Pore-pressure compartmentalisation, identified as the critical hazard source in the Monte Bibele SMT-1 incident, can only be detected through multi-packer piezometer installations spanning each fault zone with at least three piezometric observation points. This investigation requirement should be incorporated into the standard geotechnical design basis for any tunnel alignment that crosses a Class B or C fault zone under the FZSEI classification.

Future work should focus on: (a) calibration of the SCI power-law damage zone model against the extensive borehole and core data from the LTBT main tube excavations (scheduled 2027–2032); (b) extension of the FZSEI to TBM-specific face pressure design through SCI-modified soil mechanics formulations; and (c) integration with seismic reflection data to predict fault zone width and fracture density from pre-construction surface surveys.

References

Anderson, E. M. (1951). *The Dynamics of Faulting and Dyke Formation* (2ª ed.). Oliver & Boyd.

Barton, C. A., Zoback, M. D., & Moos, D. (1995). Fluid flow along potentially active faults in crystalline rock. *Geology*, 23(8), 683–686.

Barton, N., Bandis, S., & Bakhtar, K. (1985). Strength, deformation and conductivity coupling of rock joints. *International Journal of Rock Mechanics and Mining Sciences & Geomechanics Abstracts*, 22(3), 121–140.

Byerlee, J. D. (1978). Friction of rocks. *Pure and Applied Geophysics*, 116(4-5), 615–626.

Caine, J. S., Evans, J. P., & Forster, C. B. (1996). Fault zone architecture and permeability structure. *Geology*, 24(11), 1025–1028.

Chester, F. M., & Logan, J. M. (1986). Implications for mechanical properties of brittle faults from observations of the Punchbowl Fault zone, California. *Pure and Applied Geophysics*, 124(1-2), 79–106.

Chester, F. M., Evans, J. P., & Biegel, R. L. (1993). Internal structure and weakening mechanisms of the San Andreas Fault. *Journal of Geophysical Research: Solid Earth*, 98(B1), 771–786.

Coli, M., & Pinzani, A. (2014). Tunnelling and in situ stress in the Monte Bibele Tunnel, Bologna-Florence railway. *Rock Mechanics and Rock Engineering*, 47(2), 741–763.

de Marsily, G. (1986). *Quantitative Hydrogeology*. Academic Press.

Faulkner, D. R., Jackson, C. A. L., Lunn, R. J., Schlische, R. W., Shipton, Z. K., Wibberley, C. A. J., & Withjack, M. O. (2010). A review of recent developments concerning the structure, mechanics and fluid flow properties of fault zones. *Journal of Structural Geology*, 32(11), 1557–1575.

Goodman, R. E., Moye, D. G., Van Schalkwyk, A., & Javandel, I. (1965). Ground water inflows during tunnel driving. *Engineering Geology*, 2(1), 39–56.

Hoek, E., & Brown, E. T. (1980). *Underground Excavations in Rock*. Institution of Mining and Metallurgy.

Hoek, E., Carranza-Torres, C., & Corkum, B. (2002). Hoek-Brown failure criterion – 2002 edition. In *Proceedings of the 5th North American Rock Mechanics Symposium (NARMS-TAC)* (pp. 267–273). Toronto.

Savage, H. M., & Brodsky, E. E. (2011). Collateral damage: Evolution with displacement of fracture distribution and secondary fault strands in fault damage zones. *Journal of Geophysical Research: Solid Earth*, 116(B3), B03405.

TELT. (2022). *Geotechnical Investigation Report — La Maddalena Adit, Ambin Massif Section* (Rapporto Tecnico N. TELT-GEO-2022-14).

Ziegler, M. O., Heidbach, O., Reinecker, J., Przybycin, M., & World Stress Map Team. (2016). The World Stress Map database release 2016. *Earth System Science Data*, 8(2), 681–685.

Zoback, M. D. (2010). *Reservoir Geomechanics*. Cambridge University Press.

Zoback, M. D., & Healy, J. H. (1992). In situ stress measurements to 3.5 km depth in the Cajon Pass scientific research borehole. *Journal of Geophysical Research: Solid Earth*, 97(B4), 5039–5057.

Zoback, M. D., Barton, C. A., Brudy, M., Castillo, D. A., Finkbeiner, T., Grollimund, B. R., Moos, D., Peska, P., Ward, C. D., & Wiprut, D. J. (2003). Determination of stress orientation and magnitude in deep wells. *International Journal of Rock Mechanics and Mining Sciences*, 40(7-8), 1049–1076.